

Accepted Manuscript

In vivo measurement of blood clot mechanics from computational fluid dynamics based on intravital microscopy images

Olufemi Emmanuel Kadri, Vishnu Deep Chandran, Surblyte Migne, Roman S. Voronov



PII: S0010-4825(19)30001-0

DOI: <https://doi.org/10.1016/j.combiomed.2019.01.001>

Reference: CBM 3177

To appear in: *Computers in Biology and Medicine*

Received Date: 18 September 2018

Revised Date: 4 January 2019

Accepted Date: 4 January 2019

Please cite this article as: O.E. Kadri, V.D. Chandran, S. Migne, R.S. Voronov, In vivo measurement of blood clot mechanics from computational fluid dynamics based on intravital microscopy images, *Computers in Biology and Medicine* (2019), doi: <https://doi.org/10.1016/j.combiomed.2019.01.001>.

This is a PDF file of an unedited manuscript that has been accepted for publication. As a service to our customers we are providing this early version of the manuscript. The manuscript will undergo copyediting, typesetting, and review of the resulting proof before it is published in its final form. Please note that during the production process errors may be discovered which could affect the content, and all legal disclaimers that apply to the journal pertain.

**IN VIVO MEASUREMENT OF BLOOD CLOT MECHANICS FROM
COMPUTATIONAL FLUID DYNAMICS BASED ON INTRAVITAL MICROSCOPY
IMAGES**

Olufemi Emmanuel Kadri^{1,*}, Vishnu Deep Chandran^{1,*}, Surblyte, Migle^{2,*}, and Roman S.
Voronov^{1,†}

¹ Otto H. York Department of Chemical and Materials Engineering, New Jersey Institute of Technology, Newark, NJ 07102, USA

² Ying Wu College of Computing Sciences, Department of Computer Science, New Jersey Institute of Technology, Newark, NJ 07102, USA

*The first three authors contributed equally to the manuscript.

†Address correspondence to Roman S. Voronov, Otto H. York Department of Chemical and Materials Engineering, New Jersey Institute of Technology, Newark, NJ 07102, USA. Electronic mail: rvoronov@njit.edu, Fax: +1 973 596 8436, Tel: +1 973 642 4762

Abstract

Ischemia which leads to heart attacks and strokes is one of the major causes of death in the world. Whether an occlusion occurs or not depends on the ability of a growing thrombus to resist flow forces exerted on its structure. This manuscript provides the first known *in vivo* measurement of how much stress a clot can withstand, before yielding to the surrounding blood flow. Namely, Lattice-Boltzmann Method flow simulations are performed based on 3D clot geometries, which are estimated from intravital microscopy images of laser-induced injuries in cremaster microvasculature of live mice. In addition to reporting the blood clot yield stresses, we also show that the thrombus “core” does not experience significant deformation, while its “shell” does. This indicates that the shell is more prone to embolization. Therefore, drugs should be designed to target the shell selectively, while leaving the core intact to minimize excessive bleeding. Finally, we laid down a foundation for a nondimensionalization procedure which unraveled a relationship between clot mechanics and biology. Hence, the proposed framework could ultimately lead to a unified theory of thrombogenesis, capable of explaining all clotting events. Thus, the findings presented herein will be beneficial to the understanding and treatment of heart attacks, strokes and hemophilia.

Keywords Lattice Boltzmann Method; Thrombus; Blood; Simulation; Yielding; Microscopy

1. Introduction

Cessation of blood loss following vascular injuries is essential for the survival of living organisms that possess a closed high-pressure circulatory system. However, a pathological manifestation of thrombosis and embolism can potentially lead to life-threatening complications when occurring in the heart (i.e., a heart attack), brain (i.e., a stroke), or lungs (i.e., deep vein thrombosis/pulmonary embolism). Among these, thrombo-embolic infarction is the leading cause of mortality and morbidity in the United States, while stroke is the fifth[1]. Conversely, deficiencies in clotting mechanisms (hemophilia), or those due to drug interactions, can result in bleeding risks that confront surgeons on a regular basis. Yet, despite tremendous efforts by the medical research community (e.g., ~\$3 billion of annual expenditure on heart attack and brain stroke research alone[2]), the problem that essentially amounts to a clogged “pipe” remains largely unsolved to this day. Moreover, what makes one thrombus benign, while another one dangerous, is also not well understood. Therefore, understanding the mechanism behind blood vessel occlusions would be beneficial for public health, since it could improve our elucidating the risk factors involved, subsequently leading to better disease treatments and thrombectomy devices[3].

1.1. Observed Biological Heterogeneity of Thrombi Imply Mechanical Differences within their Structure

Whether an occlusion occurs depends on the ability of the growing thrombus to resist the blood flow forces exerted on its structure. With the development of advanced intravital microscopy experiments, thrombi structures have been shown to be heterogeneous (consisting of a densely packed “core” nearest the injury site and of a loose “shell” overlaying the core) (see **Fig. 1**)[4, 5]. It is also reported that the core is composed of highly “activated” platelets (as measured by P-selectin expression), while the shell consists of loosely-packed P-selectin - negative platelets. The biological purpose, as well as the cause of this heterogeneity, is unknown. One thing that is apparent, however, is that the core and the shell contribute differently to key parts of the thrombus formation and hemostasis. The shell is observed to shed the most mass (leading to the conclusion that embolism is mostly caused by this part of the clot), while the core can be seen to anchor the thrombus to the injury and stop the escape of blood to the extravascular space by “sealing” the damage. This leads to an important conclusion that there are potentially significant material and functional differences between these two regions of blood clots.

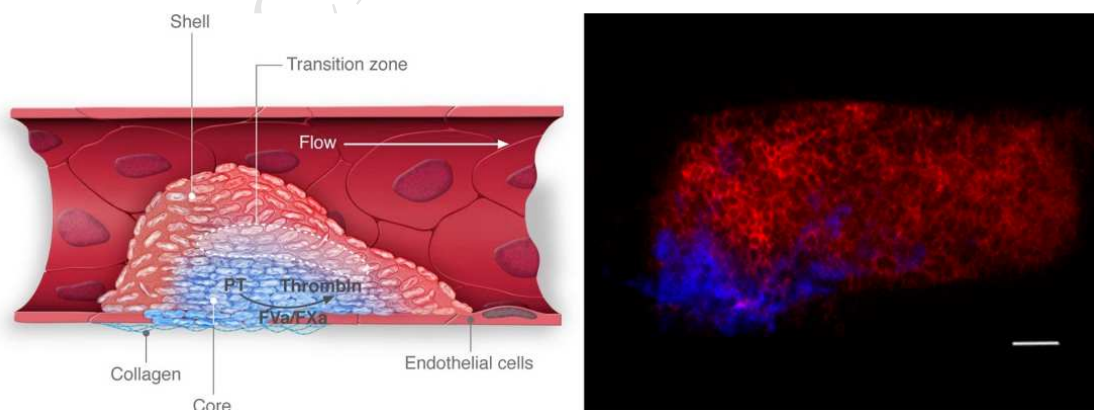


Fig. 1 LEFT - “Core-and-Shell” model schematic showing that the clot is comprised of two regions differing in degree of platelet activation and packing density; Image reprinted with permission, from Ref.[6] RIGHT – Confocal fluorescent microscopy image of a clot (Blue = P-selectin exposure marking the activated core; Red = anti-CD41 platelet marker). Scale bar is 10 μ m.

1.2. Hypothesis: Bingham-like Viscoplastic Behavior of Blood Clots

At the same time, the viscoplastic behavior exhibited by thrombi resembles that of a Bingham plastic – a material, like toothpaste, that behaves as a rigid body at low stresses but flows as a viscous fluid when its critical yield stress σ_c is exceeded (see Eqns. 1 and 2). Thus, like a Bingham plastic, the clot consists of discrete particles (in this case platelets) trapped in a liquid gel. The platelets interact with each other, creating a weak solid structure known as a “false body”. A certain amount of stress corresponding to σ_c is required to break this structure and allow the platelets to rearrange within the gel under viscous forces. After the stress is reduced, however, the platelets associate again, solidifying the thrombus’ structure. **Fig. 2** illustrates the Bingham plastic-like behavior of a blood clot as observed from intravital microscopy.

$$\dot{\gamma} = 0 \quad \sigma < \sigma_c, \text{ no flow} \quad (1)$$

$$\sigma = \sigma_c + \mu\dot{\gamma}, \quad \sigma \geq \sigma_c, \text{ flow with a constant viscosity} \quad (2)$$

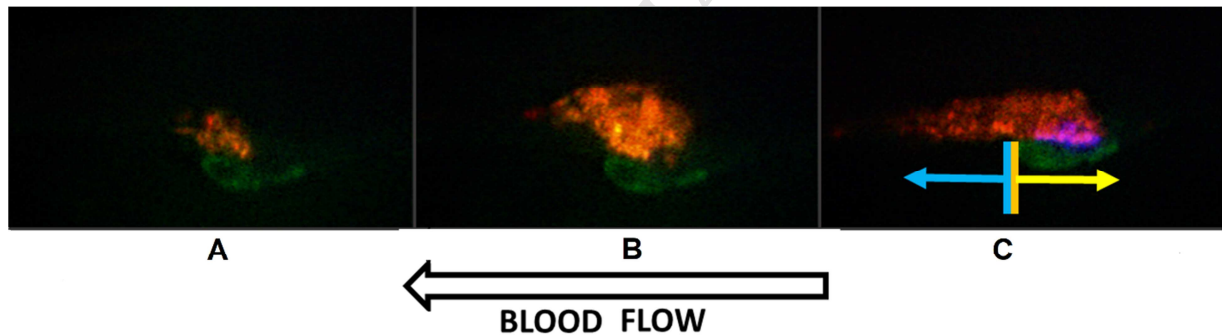


Fig. 2 Red – Platelets (Anti-CD41 platelet marker); Blue – Core (anti-P-selectin activated platelet marker); Green – Injury (Uncaged Fluorescent Albumin). White Arrow – indicates the direction of flow; Yellow Arrow – Upstream portion of the clot; Cyan Arrow – Downstream portion of the clot. A – Initial attachment to injury; B – Uniform growth prior to transition; C – Final stable steady-state core-and-shell thrombus structure, after the thrombus’ yielding to the blood flow.

The figure shows three major progression stages of a typical thrombus formation: 1) initial platelet attachment to the injury site (see **Fig. 2-A**), 2) clot growth radially outward from the injury site (see **Fig. 2-B**), and 3) steady-state stability (see **Fig. 2-C**). The transition from the second to the third stage (**Fig. 2**, panels **B**→**C**) is the Bingham-like “yielding” of the thrombus. During this critical event, platelet mass from the upstream portion of the thrombus is forced to its downstream side. As a result, the thrombus changes shape from a “ball”-like structure, to the characteristic “comet-tail” shape, typically seen in blood clots. This transition occurs that the obstructing thrombus experiences stronger forces from the surrounding fluid, which is trying to squeeze through the little remaining openings left in the lumen. Consequently, if there is no full

occlusion of the blood vessel, the thrombus' structure eventually *yields* to the flow forces and rearranges its shape to minimize the fluid drag imposed on its surface.

Interestingly, despite the underlying complexity of the thrombo-genesis mechanism, the discrete regimes shown in **Fig. 2** appear to be common to all thrombi. Therefore, it is hypothesized here that the critical yield stress σ_c is a parameter that is key to understanding the extent to which the clot's structure can resist deformation and breakage. In other words, it is an important measure of stiffness that can provide information on when the thrombus is likely to become pathogenic. Yet, σ_c remains unmeasured to this day. This is because insight into thrombo-genesis is made difficult by the fact that it is a fast small-scale process that involves a combination of coupled biochemical reaction cascades, intra- and inter-cell signaling, cell and tissue biomechanics, and non-Newtonian fluid flow[7, 8].

1.3. State-of-the-Art: Limitations of Stand-alone Experiments and Simulations

Among the experimental techniques, compression testing[9, 10], tensile testing[11-13], shear rheometry[14, 15], nano-indentation[16] and ultrasound elastography[17-19] are commonly used to estimate mechanical properties of the thrombi (e.g., elastic modulus, shear modulus, and stiffness)[9-12, 14, 16-18]. However, most of these works use *in vitro* flow loops to generate thrombi, which may not be representative of the real physiological conditions *in vivo*. For example, there are some discrepancies between *ex vivo* and *in vivo* measurements. One such discrepancy is platelet attachment, which happens so fast *in vivo*, that even high-speed cameras have trouble resolving it[20]. In contrast, the time scale of platelet activation observed *ex-vivo* are on the order of minutes, which is several orders of magnitude longer than that of *in-vivo*[21-24].

Alternatively, a preformed thrombus could be explanted from the body for an *ex vivo* measurement. However, this type of experiment corresponds to just a single time point, and only at a late stage of the thrombus formation. Therefore, it would not capture the full thrombo-genesis dynamics. Yet, this knowledge is necessary to measure the critical yield stress of the clot. Unfortunately, only a few studies among the above works measure thrombi biomechanical properties directly *in vivo*. A typical example is Mfoumou et al.[19], who used shear wave ultrasound imaging to measure thrombus stiffness in rabbits' veins. However, a) the temporal resolution of the measurements in such studies is on the order of $\Delta t = 10$ mins, which is, again, too slow to capture thrombus growth dynamics (lasts on the order of seconds), and b) the measurement occurs through tissue, which could reduce its accuracy. Therefore, better approaches are needed to reduce the ability of blood clots to resist deformation *in vivo*.

Computational models offer an attractive alternative, because they can resolve the time scale limitation by recreating thrombo-genesis *in silico*[25-32]. However, the clot structures generated by the simulations are not guaranteed to have realistic geometries or to follow a realistic deformation trajectory over time. The reasons behind these limitations are the numerous unknowns in biology. For example, simulated clot structures are typically represented using either continuum models[25, 27, 30, 32-35], discrete particle-based[26, 36, 37], or hybrid continuum/discrete particle-based[28, 29, 31, 38-40] dynamics. All these approaches rely on defining clot biomechanics via parameters such as platelet-platelet, platelet-vessel wall/injury, platelet-proteins and fibrin-fibrin bond strengths (typically modeled using simple spring constants). However, since most of these parameters are obtained from *in vitro* experimental measurements, it is difficult to verify whether they are truly representative of the *in vivo* values.

Moreover, some of the biological processes are simply too complex and consequently require numerous simplifications / assumptions for achieving bottom-up modeling. For example, platelet activation – a process central to clotting, is typically modeled using top-down neural networks pre-trained on an individual’s unique platelet phenotypes[41], while bottom-up approaches to modeling the same phenomenon require unknown-parameter estimation[42]. Therefore, the purely computational methods ultimately do not guarantee a realistic trajectory of thrombus evolution over time.

1.4. Proposed Hybrid Image-based Modeling Approach, and 3D Clot Structure Estimation

This seemingly “simple” phenomenon, which is responsible for a wide range of life-threatening pathologies, is not easily accessible to either experimental or computational inquiries alone. Consequently, semi-empirical approaches offer a reasonable compromise for overcoming these limitations. Specifically, they obtain the clot structure from experimental imaging, rather than generating it mathematically. This ensures that a realistic geometry is used for solving the physics involved in the process. For example, in Refs.[24, 30, 43, 44] such models were used to calculate the time-dependent effects of surface shear stresses on thrombi developed *in vitro*. However, as mentioned previously, *in vitro* experiments may not depict realistic physiological conditions observed *in vivo*. Hence, in Ref.[45] intravital imaging was used as the basis for calculating shear stresses in the near-thrombus region *in vivo*. However, these simulations were 2D, which may not provide quantitatively accurate descriptions of the 3D thrombus behavior. Moreover, no yield point or time-dependent stress data were reported.

The reason why the latter study was done in 2D is because the thrombus structure changes faster than a 3D confocal microscopy scan can be completed[30]. Moreover, considerable fluorophore bleaching is experienced during 3D image acquisition, even if the scanned thrombus is static. To overcome this problem, here we instead *estimate* the 3D geometry of the clots from the high-speed imaging of their cross-sections. In this manner, our image-driven simulation approach avoids the pitfalls of using either just experiments or just computation alone. To the best of our knowledge, this combination of advanced time-lapse imaging and high-fidelity computation provides the first estimate of the thrombi’s yield stress *in vivo*.

2. Methods

The overall semi-empirical approach used in this work is summarized in **Fig. 3**. Namely, the evolution of the clot structures over time is obtained from 2D intravital microscopy of laser-induced injuries in the microvasculature of live mice. Then, the 3D shape of the thrombi is estimated by casting assumptions about the relationship between the 2D and the 3D structures (based on our previous observations)[30]. Finally, Lattice-Boltzmann Method (LBM) is used to calculate the fluid forces causing the thrombi to deform (i.e., the critical yield stress σ_c).

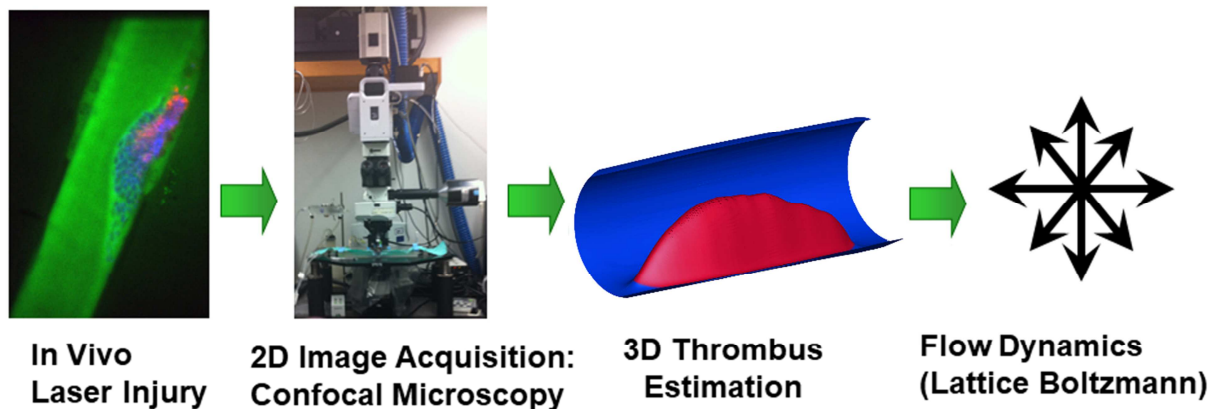


Fig. 3 Process flow diagram for the image-based modeling methodology used in this work. An injury is first induced in the microvasculature of mice to initiate thrombus formation (Blue – indicates activated thrombus core; Red – indicates thrombus shell; Green – represents lumen and interstitial space within the thrombus). Then high-resolution confocal microscopy is used for 2D visualization of the process. Afterwards, a reconstructed 3D thrombus geometry is estimated from the 2D images and imported into the LBM fluid flow solver. Finally, LBM simulation results are used to compute the shear stresses on thrombus surface.

2.1. In-Vivo Laser Injury Model and Intravital Microscopy

All of the experiments in this manuscript were performed at the Skip Brass laboratory at the University of Pennsylvania (see Acknowledgements), as described in Refs.[20, 46]. Briefly, thrombus formation was induced via laser injury of the cremaster muscle microcirculation in male C57Bl/6J mice 8-12 weeks of age (Jackson Laboratories, Bar Harbor, ME), and visualized via confocal microscopy[47]. Alexa-Fluor® monoclonal antibody labeling kits from Invitrogen (Carlsbad, CA) were used to label platelet-specific antibodies. Anti-CD41 F(ab)₂ fragments (clone MWReg30, BD Biosciences, San Diego, CA) were used to visualize both activated and quiescent platelet surfaces, anti-P-selectin (clone RB40.34, BD Bioscience) was used for specific labeling of activated platelets, and caged fluorescein conjugated to albumin[46] was used for visualizing the lumen and the laser injury site.

The center line maximum velocity of the blood flowing through the mouse blood vessels was measured using optical Doppler velocimetry, and corrected by a factor of 1.6 in order to compensate for an artifact of the measuring technique: velocity profiles appear to be slightly blunted and non-parabolic due to out-of-focus cells modulating the light intensity signals [48-50]. This procedure yielded an average blood flow velocity of 4.78 mm/s. The velocimetry measurements were taken sufficiently far away from the thrombi to ensure that the blood flow was unaffected by the presence of the thrombi. Additional details on the experimental procedure can be found in our prior publications[4, 46]. All of the procedures and protocols were approved by the Institutional Animal Care and Use Committee (IACUC) of the University of Pennsylvania.

2.2. 2D Image Acquisition, Post-Processing and 3D thrombus Shape Estimation

Since 3D imaging is too slow to capture clot shape changes, 2D images from the confocal microscope were acquired using SlideBook 5 software (Intelligent Imaging Innovations) with a

time interval of 0.619 seconds and a spatial resolution of $0.22 \mu\text{m}/\text{pixel}$. A total of 300 time images were collected for every experiment. The obtained images were deblurred using a technique reported in Ref.[20]. Next, Fiji[51] plug-ins were used to compensate for vibrations due to muscle contractions in the mouse and air currents surrounding the sample. Specifically, to achieve video stabilization, all intensity channels were superimposed together, and stabilized collectively using either StackReg[52] or Image Stabilizer ImageJ plug-ins[53], where the choice of plug-in is based on which gave better results for each particular capture. Finally, a custom Matlab code (MathWorks Inc., Natick, MA) was used to further enhance the signal-to-noise ratio of the 2D images and subsequently segment 2D thrombus shapes using standard image processing techniques.

Once the 2D images were post-processed, an in-house Matlab code (MathWorks Inc., Natick, MA) was used to generate *estimated* 3D clot geometries based on the 2D confocal images at each time point. Specifically, the code assumed that each time-point image represented longitudinal (i.e., *parallel* to the blood flow axis) 2D cross-sections through the center of the *actual* 3D thrombi at that same instant. This is a good assumption, since the microscope's operator particularly chose an imaging plane such that the thrombi's cross-sections were maximized. A representative grayscale thrombus cross-section from microscopy is shown in **Fig. 4-A**. Subsequently, cross-wise (i.e., *perpendicular* to the blood flow axis) parabolic cross-sections were stacked along the "spine" of each clot artificially to estimate the thrombi's 3D shapes (see **Fig. 4-B**).

The distance between the consecutive parabolic slices corresponded to the microscopy image resolution of $0.22 \mu\text{m}$ (or one lattice spacing in LBM units). The resulting parabolic shape, chosen to represent the outer thrombus perimeter, was selected based on experimentally-observed 3D reconstructions of a static clot[20]. Specifically, the height of each parabola was dictated by the height of thrombus' "spine" at every position along the *longitudinal* direction, while the widths of the parabolas were assumed to be in a constant 2:3 ratio with the parabola heights throughout the thrombus. This ratio was again consistent with experimental observations from static 3D *in vivo* imaging shown in Ref.[20].

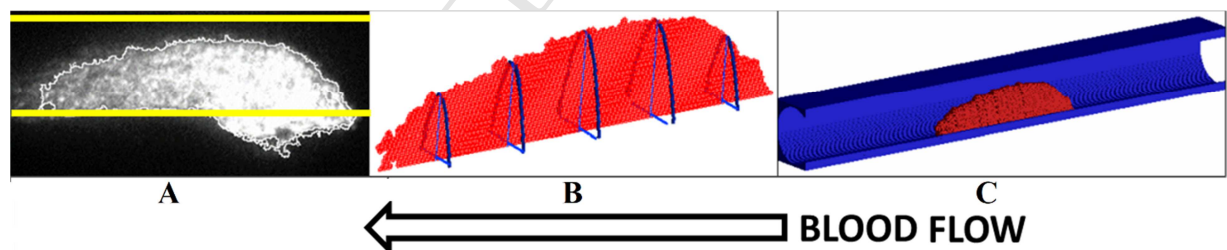


Fig. 4 3D Thrombus Shape Estimation Procedure: A – a 2D grayscale image of a thrombus cross-section obtained via confocal fluorescent microscopy (yellow lines mark the blood vessel edges); B - illustration of how parabola are fit on the edges to generate 3D geometry (red is the 2D cross-section, blue are the parabolas fitted to its "spine"); C - resulting 3D reconstruction (blue is a pipe fitted around thrombus depicting the blood vessel; red is the estimated thrombus). Pipe diameter and lengths are 0.03685mm and 0.2275mm for this experiment, respectively. The white arrow indicates the direction of blood flow.

Finally, the blood vessel walls were manually segmented from the 2D images to measure the lumen diameter. Subsequently, a 3D pipe of the same size was created around the estimated 3D

blood clot (see **Fig. 4-C**). The length of the pipe was chosen to be three times the maximum clot length to avoid entrance effects in fluid flow simulations.

2.3. Fluid Flow Modeling: Lattice-Boltzmann Method (LBM)

Convection within the blood vessels and around the 3D thrombi was modeled via LBM. This is a numerical technique often implemented for simulating mesoscopic fluid flows, which consists of solving the discrete Boltzmann equation[54-56]. Additionally, it has many computational advantages, such as inherent parallelizability[57, 58]. Furthermore, LBM techniques have been implemented in a wide range of complex fluid dynamics applications, such as turbulence[59], non-Newtonian flows [60-62], and multiphase flows [63]. Moreover, it has recently gained popularity for modeling biological flows[64-71], due to its ability to the ease with which it handles complex boundary conditions on supercomputers[72]. Both of these aspects make the method especially attractive for dealing with the high-resolution microscopy images, such as the ones used in this study.

An in-house code[20, 64, 66-69, 73-75] was used for this work. Its solver uses a D3Q15 lattice[76], in conjunction with the single-relaxation time Bhatnagar, Gross and Krook[77] collision term approximation, in order to model the flows. The no-slip boundary condition was applied at wall faces of the blood vessels and the thrombi using the “bounce-back” technique[55]. The simulation domains were decomposed using the message passing interface (MPI) in order to distribute the computation across a cluster of computers [64, 69]. The code has been previously validated against several analytical solutions of flows in different geometries: slit, pipe and an infinite array of spheres[64, 68].

The LBM simulations were performed for a total of ten different laser-injury experiments (see **Table 1**). For each one, a *pseudo steady-state* approach was taken to update the clot shape based on the successive microscopy images. Namely, flows through geometries representing each individual time step were solved *separately* from each other, as *steady-state* simulations. Ultimately, the individual time step results were then concatenated to form a continuous time-series. The pseudo steady-state approach is a good assumption, given that the fluid velocity field changes much faster than do the clot geometries.

Table 1 Summary of experimental measurements and simulation results for the 10 modeled thrombi.

Blood Vessel Diameter [μm]	Maximum stress (dynes/cm ²)		Maximum				Specific Surface Area [μm ² /μm ³]
	Constant Pressure Drop	Constant Flow Rate	CD41 Area[μm ²]	P-Selectin Area[μm ²]	CD41 Volume[μm ³]	Injury length[μm]	
28.30	57.12	92.68	749.89	82.98	4447.79	27.23	55838.42
34.18	55.57	81.23	1580.69	137.87	10922.70	25.63	39835.00
30.44	54.27	56.16	447.91	107.58	906.50	13.88	58685.18
34.71	55.83	93.32	1333.18	180.93	10881.41	36.31	50712.37
36.85	51.40	82.88	1759.63	170.45	16455.41	26.17	39182.72
41.12	44.23	61.67	1313.43	183.64	9818.34	26.97	53490.24

42.19	43.43	76.78	1755.28	174.02	17243.75	30.97	54409.11
51.26	33.28	33.80	2037.72	201.61	13299.55	50.46	37391.42
57.67	27.58	30.80	2297.07	173.66	17016.10	41.39	46383.00
45.92	35.43	48.89	2742.20	180.72	21660.17	59.81	43235.64

While the fluid dynamic viscosity of blood is known to be shear-dependent[78, 79], here it is assumed to be a Newtonian fluid a viscosity of $\mu \approx 0.03$ gr/cm-s (which corresponds to a kinematic viscosity of 0.167 in LBM units)[80, 81]. This is considered to be a good approximation due to the low hematocrit typically observed in microvasculature[82], such as the cremaster muscle. Given that the reality is likely to be something in-between, two different boundary conditions commonly encountered in literature were modeled: constant pressure drop [25, 44, 83] and constant flow rate[44, 84]. For the latter, the flow is continuously adjusted to ensure that input flow rate is maintained consistently throughout thrombus development. In both cases, the *initial* average lumen blood velocity in LBM was matched to the *in vivo* value of 4.78mm/s. This measurement was obtained by optical Doppler velocimetry for a comparable diameter blood vessel (as discussed in the experimental methodology Section 2.1). The simulations were considered to be converged when the minimum, average, and maximum flow velocities in the whole domain varied by less than 0.01% per LBM 1000 steps. Approximately 60,000 steps, corresponding to 3.96×10^{-9} seconds each, were needed for a full conversion of every experimental time step. The image-based LBM simulation results were validated against an idealized homogeneous porous media model of a thrombus using a commercial computational fluid dynamics package COMSOL® (Discussed further in Section 4).

2.4. Stress Calculations

The fluid-induced shear stresses acting on the thrombi surfaces were estimated using Eqn. 3[65]:

$$\underline{\underline{\sigma}} \approx \mu \left(\frac{1}{2} \right) (\nabla U + \nabla U^T) \quad (3)$$

Where $\underline{\underline{\sigma}}$ is the shear stress tensor and U is local velocity vector.

Derivatives of the velocity field given in Eqn. 3 were approximated numerically using the 1st order centered finite difference approximation (Eqns. 4 – 6). The same was done for the velocities in the other directions, U_y and U_z :

$$\frac{\partial U_x(i, j, k)}{\partial x} = \frac{U_x(i + lu, j, k) - U_x(i - lu, j, k)}{2 \times lu} \quad (4)$$

$$\frac{\partial U_x(i, j, k)}{\partial y} = \frac{U_x(i, j + lu, k) - U_x(i, j - lu, k)}{2 \times lu} \quad (5)$$

$$\frac{\partial U_x(i, j, k)}{\partial z} = \frac{U_x(i, j, k + lu) - U_x(i, j, k - lu)}{2 \times lu} \quad (6)$$

Where lu is the length of one side of an element in the LBM model.

Following this, the symmetric strain matrices for every node in the simulation were found by summing the 3×3 partials matrix with its own transpose. The eigenvalues of the symmetric matrix were then found using the Jacobi method, and the largest absolute-value eigenvalue was used to determine the fluid-induced shear stress on the thrombi surfaces. Furthermore, the upstream wall stress obtained using this procedure was ~ 31 dyn/cm², which is comparable to the experimental value of 40 dyn/cm² reported in literature[85]. 3D reconstructions of the simulation results were generated using Tecplot 360 EX 2017 (Tecplot Inc., Bellevue, WA USA) in order to visualize the velocity and stress distributions acting on and around the thrombi.

3. Results

The material properties of thrombi provide a measure of when the clots can potentially become pathological. The goal of this paper is to *estimate* the mechanical strength of the thrombi formed in the microcirculation of live mice. This is done by calculating the stresses induced on the clot by the surrounding blood flow, from LBM simulations based on intravital microscopy images. The hybrid semi-empirical approach helps to overcome limitations of conventional experimental and simulation tools: such as, the inability to do fast 3D fluorescent imaging in case of the former, and the uncertainty in generating the thrombi structures mathematically, in case of the latter.

3.1. Nondimensionalization via Data Normalization

Firstly, it was found that although each clot has unique properties (such as size, morphology, formation kinetics, etc.), the evolution of different thrombi looks similar when compared on a dimensionless scale. Therefore, to normalize the data from all clots to the same scale, we nondimensionalized the experiment time by dividing it by a “characteristic” one. This is shown in Eqn. 7:

$$t^* = t/t_{char} \quad (7)$$

where t^* is the dimensionless time, t is the experiment time, t_{char} is some characteristic time.

To define the latter, we used the time at which the blood clot’s size is maximal, because obtaining this value does not require any complicated analysis or performing simulations. The thrombus size was quantified via the *area* of the anti-CD41 platelet marker fluorescence in the microscopy images.

The ordinate values for the data analyzed in this manuscript are also normalized using the corresponding maximal values. For example, the normalization for the clot area is as follows

$$A^* = A / A_{max} \quad (8)$$

where, A^* is the dimensionless clot area, A is the clot area measured from the anti-CD41 marker’s fluorescence, and A_{max} is the peak value of A (obtained as shown in **Supplemental Fig. 1**).

3.2. Distinct Regimes of Thrombogenesis

In order to identify different stages of thrombogenesis, we plotted the mean dimensionless thrombus area as a function of the normalized time (see *red* curve in **Fig. 5**). Additionally, we plotted the mean aspect ratio (AR) for the same clots (see *blue* curve in **Fig. 5**), in order to characterize changes in their morphology. The AR is defined as the clot height divided by the clot length, and is measured based on the shape of the anti-CD41 fluorescence. However, since it is already dimensionless, the AR is plotted against the dimensionless time without normalization.

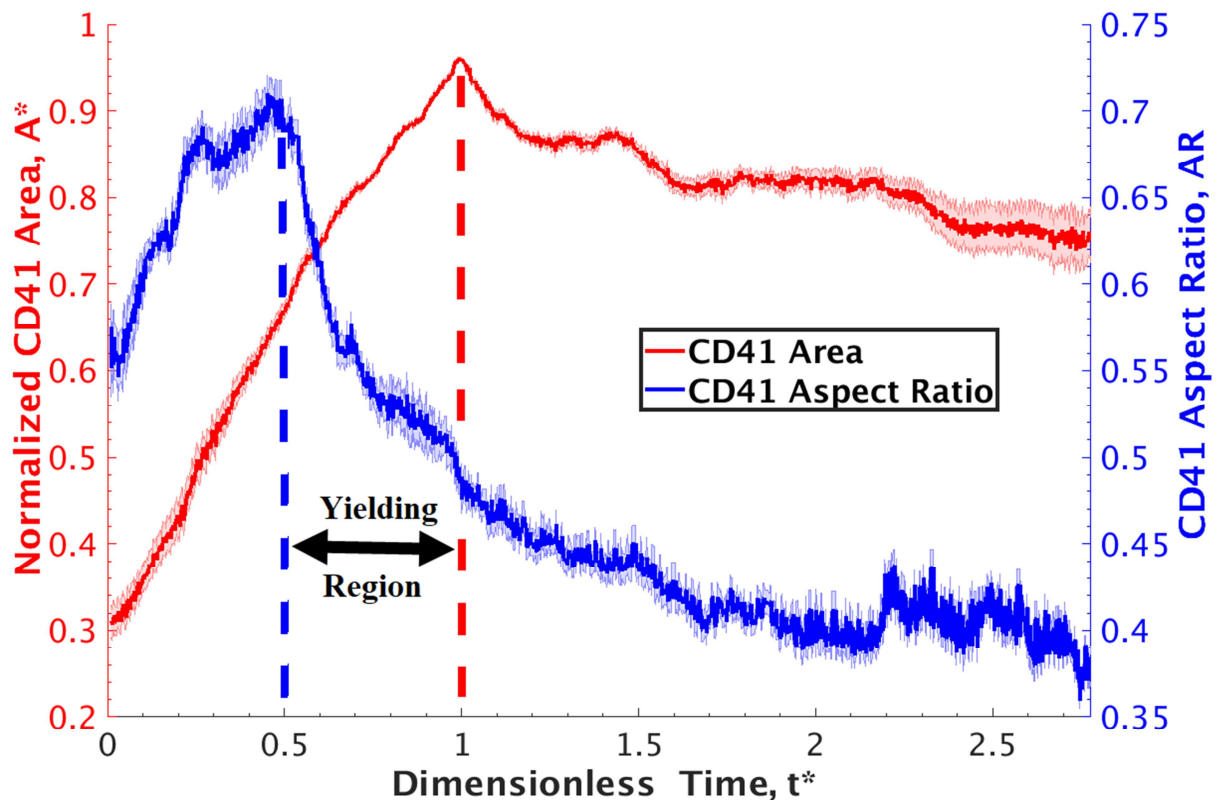


Fig. 5 Data nondimensionalization strategy: The red graph shows the clots cross-sectional size, quantified based on the anti-CD41 marker area in the microscopy images. The blue graph shows the clot's aspect ratio = height / length. Abscissa is the dimensionless time, whose unity corresponds to the peak CD41 area in the red color curve. Both curves are moving averages with a window of 0.5, and the error bars represent the moving variance for the 10 experiments in **Table 1**.

Several observations regarding the mechanism of thrombogenesis can be made from **Fig. 5**. Here, we separate them into three distinct stages, each of which describes unique characteristics of the clots evolution:

Stage I – Uniform Growth Regime: $0 < t^* \leq 0.5$

During this period, both the height and the length of the clot increase simultaneously (see the *red* curve in **Fig. 5**). However, it is evident from the upward trend in AR (see the *blue* curve

in **Fig. 5**) that the clot's growth in the vertical direction outpaces that of its horizontal elongation. The reason for the mismatch is owed to the differences in the mechanisms by which the clot dimensions change. Specifically, the length grows due to platelets attaching to the injured portion of the blood vessel wall. However, the availability of unoccupied sites in this injured region is limited, since the cells cannot attach to the undamaged parts of the blood vessel. This restricts the horizontal growth to the span of the injury. At the same time, the vertical growth remains unhindered, because the activated platelets can attach on top of each other as the clot builds. Consequently, the cells pile up faster vertically than they do horizontally during this stage of thrombogenesis. The described behavior continues up until approximately $t^* = 0.5$, which is considered to be the upper bound of the Stage I regime.

Stage II – Hindered Growth / Structure Yielding Regime: $0.5 < t^* \leq 1$.

The boundary between this regime and the previous one is marked by the peak in the AR at $t^* = 0.5$ (see the *blue* curve in **Fig. 5**). We define this point as the beginning of Stage II, because this is the time at which the growth in the vertical direction begins to slow down. The lag happens because the thrombus begins to occlude the lumen and as a result, the platelets have to overcome increasingly stronger fluid flow forces in order to attach to the top portion of the clot. In contrast, the growth in the horizontal direction remains unaffected, and continues at the same rate as it did during Stage I. This happens because the platelet mass is gradually transferred from the upstream side of the clot to its downstream side, resulting in the formation of a “tail” that extends beyond the injury site.

In other words, the thrombus experiences the yielding of its “false body”. This is signified by a decrease in the AR – a measure of the clot's deformation. In fact, the majority of the AR's decrease occurs during Stage II, as is evident from the negative values of dAR/dt^* between $t^* = 0.5$ and 1 (see **Supplemental Fig. 2**). Ultimately, the end of this regime is marked by the thrombus reaching the peak size (see the *red* curve in **Fig. 5**), which it can sustain while opposing the blood flow forces. Consequently, the clot's structure finishes the yielding, as t^* approaches the value of unity. For this reason, we choose the time $t^* = 1$ as the critical point used to mark the upper bound of Stage II.

Stage III – Structural Stabilization / Mass Shedding Regime: $t^* > 1$

The beginning of Stage III is marked by two distinct events, both of which occur for the first time since the initiation of the thrombogenesis process: 1) the clot size begins to decrease (see the decline of the *red* curve in **Fig. 5** after $t^* = 1$); and 2) the clot length and height start to change in the opposite directions (see **Supplemental Fig. 3**).

Specifically, the clot height starts to decrease while the length continues to grow. These phenomena are primarily caused by the fact that the thrombus structure has yielded and rearranged into the elongated “comet-tail” shape, which is characteristic of stable clots. Furthermore, given the streamlined shape, there is more surface area available for the drag forces to pull on and extend the clot even further. Finally, the mass shedding continues to facilitate the decrease in the clot height, as the platelet cells are removed by the blood flow from the top of the thrombus.

This interplay between the flow forces and the clot structure continues in the pseudo-equilibrium fashion, as the clot slowly thins out and stretches out. Ultimately, it retracts towards the injury site, in order to seal the damage and prevent the escape of blood into the extravascular. Overall, the time points t^* equal to 0.5 and 1 appear to be physiologically

characteristic of the transitions between the distinct process stages of the thrombogenesis process.

3.3. Clots Experience Heterogeneous Deformation During Yielding

Interestingly, the thrombus' inner region (i.e., the "core") does *not* show a similar trend of deformation as does the shell. **Fig. 6** shows an analysis of the cores' morphology, analogous to **Fig. 5**. Namely, this figure plots the core's P-selectin area and aspect ratio on the same dimensionless time scale, t^* . The core's area is also normalized according to Eqn. 8, where the peak value A_{\max} is obtained as shown in **Supplemental Fig. 4**.

Similar to the overall thrombus growth shown in **Fig. 5**, the core increases in size up until $t^* = 1$, after which it stays about the same size. Physiologically, the core's growth corresponds to the activation of the platelet mass nearest the injury, similar to what was shown in **Fig. 1**. However, unlike the overall thrombus shape, the core's aspect ratio remains unchanged throughout the whole formation of the clot. From this, it can be concluded that most of the clots' deformation occurs in the only thrombus' outer region (i.e., in the "shell"), where loosely bound platelets are re-arranged in response to fluid flow stresses.

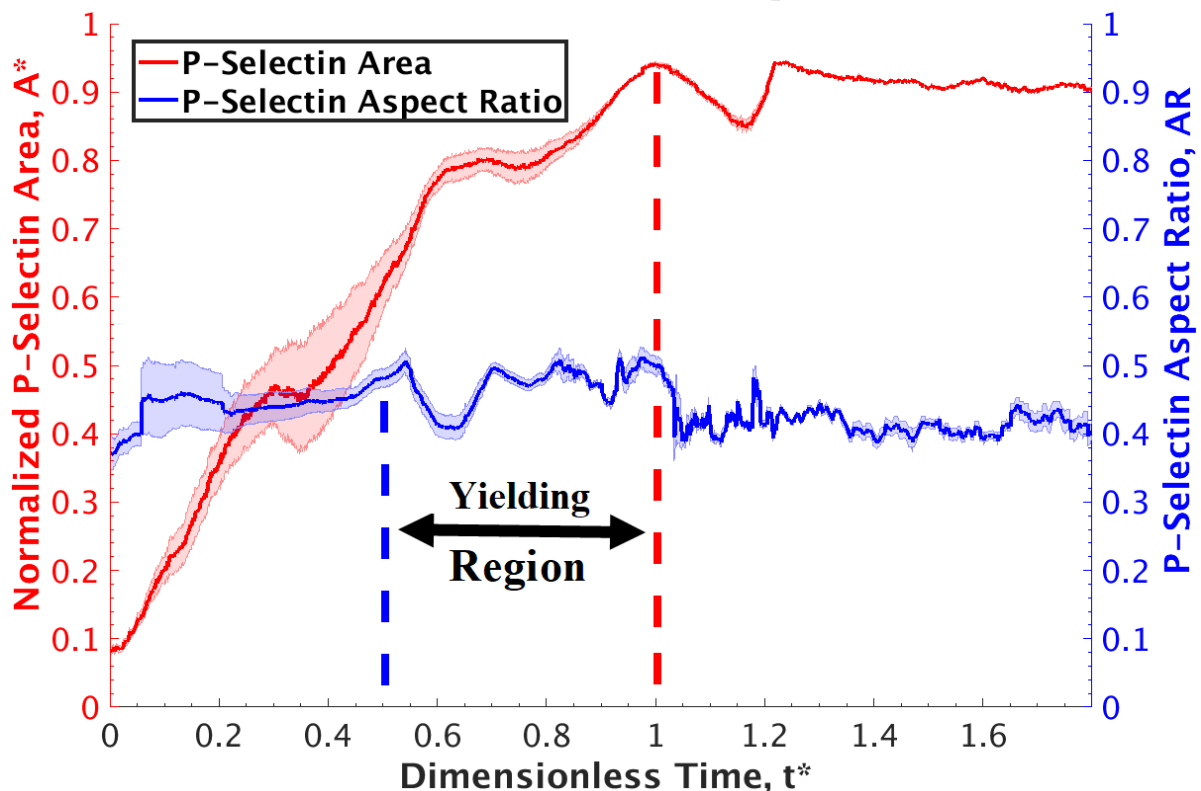


Fig. 6 Changes in nondimensionalized thrombus' core size and morphology, plotted as function of normalized time. Red graph shows the core's cross-sectional size, quantified based on the anti-P-selectin marker area in the microscopy images. Blue graph shows the core's aspect ratio = height / length. Abscissa is the dimensionless time; whose unity corresponds to the peak CD41 area in the red curve in **Fig. 5**. Both curves are moving averages with a window of 0.5 and the error bars represent the moving variance for the 10 experiments in **Table 1**.

3.4. Image-based Modeling of the Fluid-induced Stresses Imposed on the Clots

Since the thrombus partially obstructs blood flow within the vasculature, the thrombus structure experiences forces exerted onto it by the passing fluid. These forces can drive thrombus break-up and embolism. Additionally, platelet adhesion and aggregation [86] and activation [87, 88] are influenced by local shear rate. Hence, we wanted to correlate the manner in which the fluid-induced stresses that the thrombi experience due to the flow in the blood vessels affect their deformation. To do this, we reconstructed the 3D thrombus shapes, estimated from the intravital microscopy images, in a virtual blood vessel (procedure in **Section 2.2**). Once the clot geometry was obtained, an in-house LBM code was used to calculate the blood velocity field established around the thrombi versus dimensionless time (see **Supplemental Fig. 5** and **Video 1**).

This figure shows how the velocity changes for a typical thrombus, under the *constant pressure drop* boundary conditions. In this case, the blood flow around the clot *decreases*, as the growing thrombus creates a larger and larger resistance to the flow. This is because at a constant pressure drop, it is more difficult to overcome the growing resistance of the thrombus protruding into the center of the lumen.

Conversely, in the case of the *constant flow rate* boundary condition (not shown), the velocity would *increase* to push the same amount of fluid through a narrower opening in the lumen. As discussed previously in Section 2.3, we performed both types of the simulations, to obtain the upper and lower bounds of the stress experienced by the thrombi. This is because the physiological reality is likely to be something in between the two boundary conditions: namely, a) an injured blood vessel tends to relax in order to avoid occlusion (similar to the *constant pressure drop* case), b) blood may get re-routed through other pathways in the vasculature (similar to the *constant pressure drop* case), and c) the heart may compensate in order to clear the obstruction by pushing the blood harder (similar to the *constant flow rate* case).

Ultimately, the LBM velocity fields for both boundary condition types were used to calculate the fluid-induced stresses experienced in the lumen, using the procedure described in Section 2.4. A representative result for the *constant pressure drop* boundary condition is shown in **Fig. 7** and **Video 2**. As expected, the stress distributions change with time, due to the effects that the evolving thrombus structure has on the surrounding blood flow in the lumen. As validation, the thrombus base (nearest the blood vessel wall) experienced stresses comparable to the value of ~ 31 dynes/cm², which is expected for an empty blood vessel of a similar diameter (calculated using Hagen–Poiseuille equation)[89]. Moreover, these values are also comparable to the experimentally measured values of ~ 47 dynes/cm² for arterioles of similar sizes to cat mesentery[85]. Finally, the top part of the thrombus protrudes into the center of the blood vessel, and experiences stresses that are several fold higher than are imposed on its base. Hence, the highest flow forces are acting on the shell of the thrombus, rather than on the core. This is consistent with the shell being the part of the thrombus that experiences the most deformation.

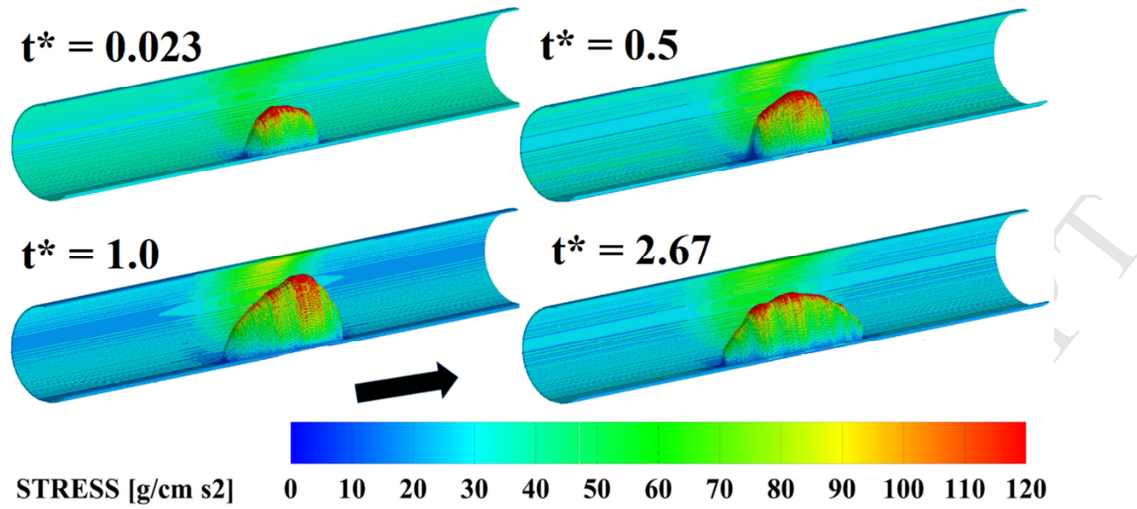


Fig. 7 “Heatmap” of the LBM fluid-induced surface shear stress, calculated using the constant pressure drop boundary condition. The results are shown at different time points. $t^* = 0.023$ is an earlier time in the thrombus formation process; $t^* = 0.5$ is the time marking the beginning of deformation/yielding; $t^* = 1$ is the time marking the end of deformation/yielding, when significant mass is transferred to the back of the clot; $t^* = 2.67$ is a later time after thrombus yielding during which thrombus has assumed its final shape. The black arrow indicates direction of blood flow.

Next, the stresses were plotted as a function of the dimensionless time t^* , and normalized as follows:

$$\sigma^* = \sigma / \sigma_{\max} \quad (9)$$

where, σ^* is the dimensionless fluid-induced shear stress, σ is dimensional fluid-induced shear stress, and σ_{\max} is the peak value of σ (obtained as shown in **Supplemental Fig. 6**).

Furthermore, since the simulations are computationally expensive, only every 10th-time step out of the total 300 was modeled for each experiment. However, we did solve one of the experiments fully, confirming that the obtained trends would be similar. This confirmation is shown in **Supplemental Fig. 7**.

From this figure, it is apparent that solving every 10th time step is sufficient to capture the stress trends displayed by the thrombi. Hence, the time-coarsed stress results are shown in **Fig. 8**.

In **Fig. 8**, the normalized stresses are averaged over the thrombi surfaces, and plotted versus the normalized time, for both the *constant pressure drop* and *constant flow rate* scenarios. In both cases, as the thrombi grow in the blood vessel, the shear stresses imposed on their surfaces initially increase with time. However, the locations of the peaks do not coincide. Instead, they are located approximately at the beginning ($t^* = 0.5$) and the end ($t^* = 1$) of the clot’s “yielding region”, for the *constant pressure drop* and *constant flow rate* cases, respectively. This again, supports the notion that the two boundary conditions represent extreme cases, while the reality is likely to be something in-between. Furthermore, it is worthy of noting that in the limit of long time, the stresses decrease roughly to their initial values, while the clot

sizes remain nearly constant after peaking. This supports the notion that the thrombi shape rearrangements are driven by drag minimization.

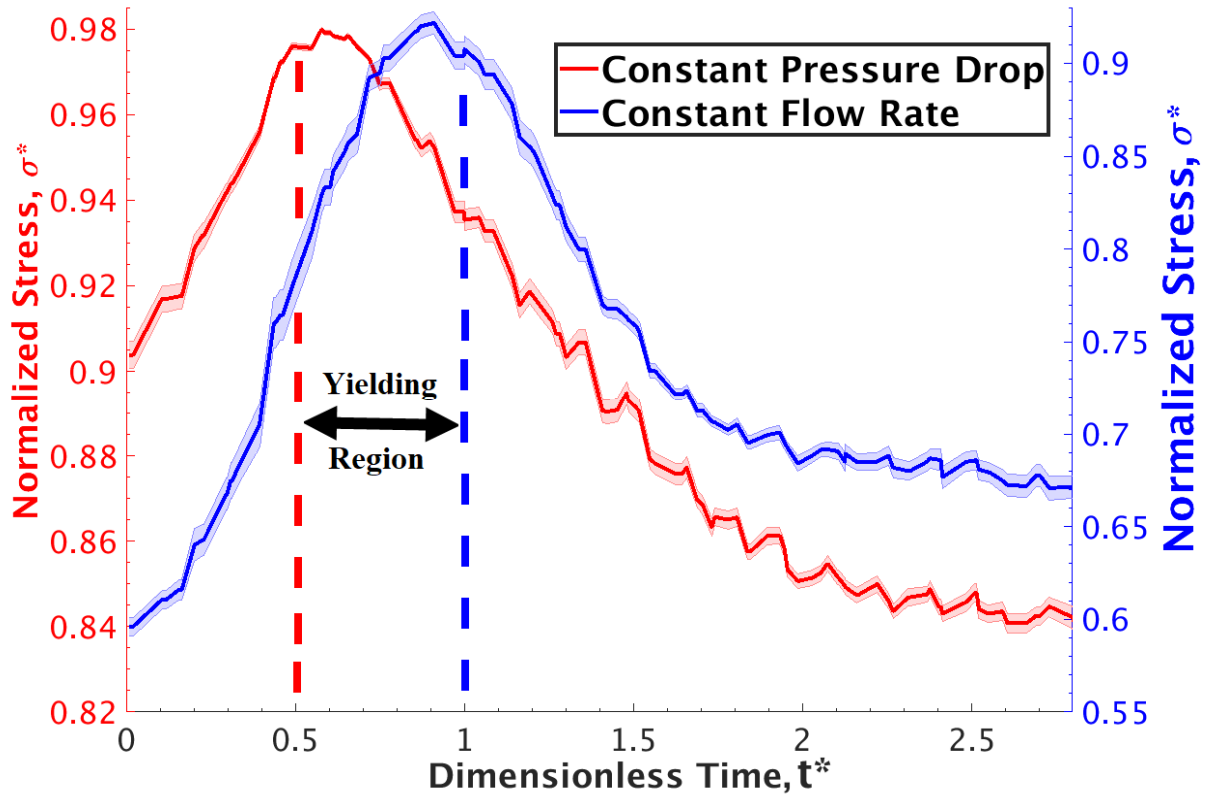


Fig. 8 Normalized stress data averaged over the thrombus surface, and plotted as a function of normalized time. Blue curve represents *constant flow rate* simulation results. Red curve represents *constant pressure drop* simulation. Abscissa is the dimensionless time; whose unity corresponds to the peak CD41 area in the red color curve in **Fig. 5**. Both curves are moving averages, with a window of 0.5; and the error bars represent the moving variance for the 10 experiments in **Table 1**.

Finally, **Table 1** catalogues the σ_{max} values for the 10 thrombi modeled in this study. These can be used to recover the actual (i.e., dimensional) stresses from the dimensionless curves in **Fig. 8**. Additionally, the σ_{max} results can be extrapolated to other blood vessel sizes. For example, we have observed a strong dependence of the yield stresses on the blood vessel diameter (see **Fig. 9**).

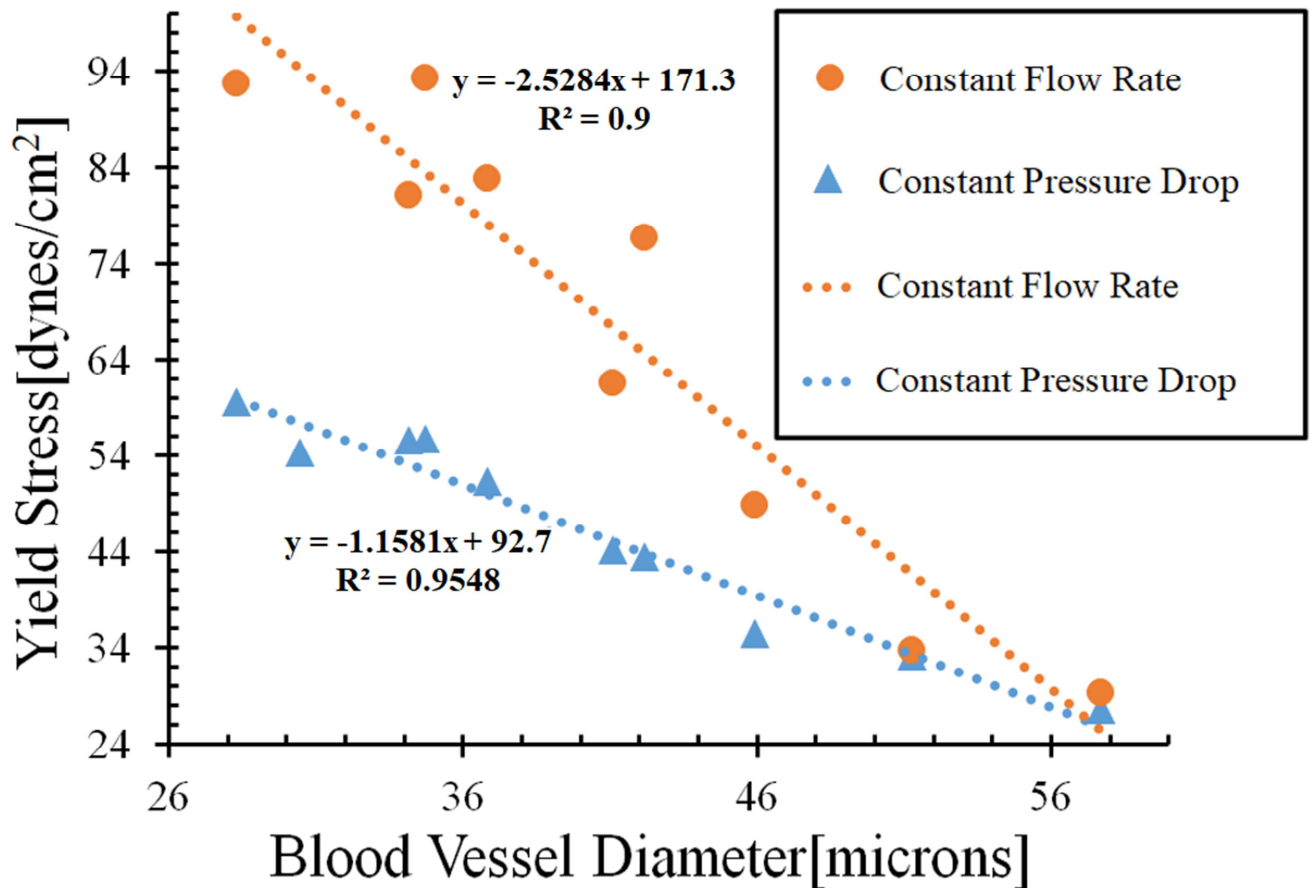


Fig. 9 Yield Stress as a function of Blood Vessel Diameter: solid markers indicate LBM calculations, while dashed lines are linear least squares fits through the data.

Although, this may seem surprising at first, it appears that geometric attributes of the blood vessel dictate the peak size of the thrombi. Specifically, the maximum clot volume was found to vary with the blood vessel diameter and injury length (see **Fig. 10**). Consequently, it makes sense that the clots found in different blood vessels can withstand varying amounts of stresses, depending on how big or small their structures are.

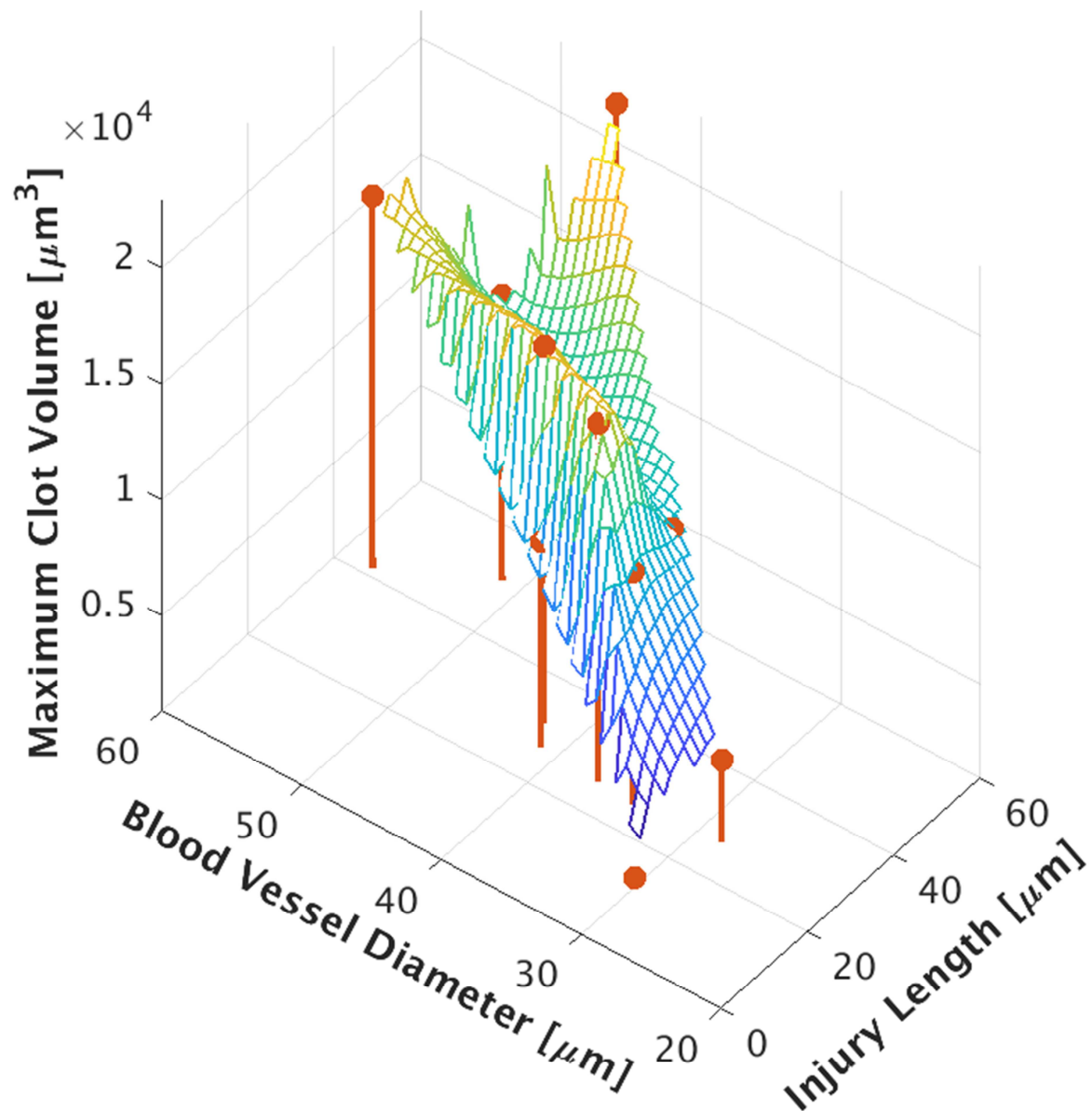


Fig. 10 Dependence of clot size on blood vessel diameter and injury length. Red “stems” represent the 10 experimental measurements from this study, while the colored mesh is a fit through these points (meant to serve as a guide for the eye).

4. Discussion

The yield stress is a critical property representing the mechanical strength of the thrombi material; as such, it provides a measure of when a blood clot can potentially become pathological. Therefore, quantitative characterization of this parameter is important to public health. However, it is difficult to measure *in vivo* by using either purely experimental or purely computational tools alone. Hence, we applied a semi-empirical framework that combined intravital imaging and flow dynamics simulations, to overcome the technological challenges of the conventional approaches. To the best of our knowledge, this is the first measurement of the

thrombi' critical yield stress made *in vivo*. Expectedly, our stress results compare well with both the 2D *in vivo* stress calculations (see **Fig. 4** in Ref. [45]) and, the 40 dyn/cm² *in vitro* value for “dynamic” elastic modulus of less activated platelet aggregate (see Table 1 in [33]).

Moreover, we have reported that the thrombo-genesis mechanism appears to consist of several discrete regimes that are common to all clots irrespective of the underlying uniqueness and complexity of their formation. Consequently, we identified the time of the clot yielding to be a characteristic nondimensionalization parameter, which appears to coincide with both mechanics (e.g., the clots stop growing after the end of yielding at $t^* = 1$) and biology (e.g. P-selectin expression in the core plateaus at $t^* = 1$) of thrombi formation. Hence, we showed that it can be used to collapse data from multiple injury events onto a single master curve. Furthermore, the consistency of the nondimensionalized trends across the multiple blood vessel injuries gives hope that a uniform theory of thrombo-genesis can be developed, which would be able to describe all clotting events using a single analytical expression.

Finally, we showed that the thrombus core does not change shape appreciably. In contrast, the shell experiences significantly higher fluid-induced stresses, which result in its deformation. This raises the likelihood that the shell is an inherently compromised part of the clot (the high shear stresses may facilitate shell fragmentation due to mechanical disturbance); and that as such, it is responsible for most of the embolism. Hence, it can be concluded that the core is structurally stronger, and that it tethers the overall body of the thrombus to the injury. Consequently, the biological differences between these thrombi regions could mean that it is possible to dissolve just the dangerous part of the blood clot (i.e., the embolizing shell), while leaving the useful one (i.e., the core which seals the injury) intact. In this manner, a new generation of drugs could be developed that would selectively target just the shell, thereby avoiding the dangerous bleeding complications from the medications currently available on the market.

Although our study provides important information regarding the thrombus biomechanics, it is necessary to keep in mind that it is only an *estimate* and that several assumptions and simplifications had to be made to obtain it. Specifically, the *limitations* of this study are as follows: 1) The 3D shapes of the clots were extrapolated from their 2D longitudinal cross-sections, by assuming that the crosswise profiles of the thrombi are parabolic in shape and have a constant width-to-height ratio (see **Fig. 4-B**). Although this was measured experimentally[20], a late-stage *static* thrombus was used. Hence, this assumption may not work well for the very early stages (i.e., $t^* < 0.5$) of the thrombus formation (when the clot has a less elongated shape). However, this only concerns the 3D LBM simulations, while the 2D experimental results would not be affected; 2) The pseudo steady-state approach to the simulation necessitated the assumption that the velocity field of the blood flow establishes faster than the clots change their shape. This was considered to be a good assumption, because the total simulation time needed to converge a single LBM model of an experimental time step was significantly faster than the microscope's image acquisition increment time: $\sim 2.38 \times 10^{-4}$ vs 0.619 seconds, respectively; 3) The thrombi are assumed to be impermeable to the fluid flow, since the true nature of their porous structure could not be approximated using our minimalistic approach. However, COMSOL® validations showed that making the clot permeable has a negligible effect on the stress results (see **Supplemental Fig. 8**).

Furthermore, we confirmed that the idealized COMSOL® model gives stress trends similar to those obtained via image-based LBM (compare **Supplemental Fig. 9** to **Fig. 8**);

4) We did not model blood escape from the injury site, which could cause the simulated flow field to deviate from the real one; 5) The shape of the blood vessel was assumed to be a straight solid pipe, while in reality it may bend and deform, (especially near the injury site); 6) Finally, the blood was assumed to be a Newtonian fluid for simplicity. However, this is commonly done in similar thrombo-genesis modeling studies[20, 24, 43, 90]. Moreover, any inaccuracies incurred due to this assumption are believed to be small, since blood behaves close to a Newtonian fluid when the shear stress is larger than 1 Pa (which is our case)[45].

The future directions for this work include performing similar measurements of the blood flow forces experienced by occlusive and embolizing thrombi (both of which are harder to induce and capture experimentally). Furthermore, we plan to continue working towards developing a universal model of thrombo-genesis. This will be done by correlating other physiological phenomena, such as the dynamics of the blood's escape to the extravascular space, to the dimensionless time scale, t^* . Additionally, the "plastic viscosity" (in the second term on the right-hand side of Eqn. 2) will be measured via image-based modeling). Finally, superior imaging methods will be used to capture the real-time 3D thrombi shape changes, instead of relying on extrapolations based on the 2D cross-sections from conventional confocal microscopy.

5. Conclusions

In this study, we have performed an in-depth analysis of intravital microscopy images, showing thrombi development in response to laser-induced injuries in live mouse microvasculature. Based on these results, we were able to conclude that the thrombus core does not change shape appreciably during thrombo-genesis, but its shell does. This implies that there are inherent differences in the material properties of these two regions of the clots. Furthermore, we performed image-based LBM modeling that allowed us to calculate the fluid-induced shear stresses imposed on the thrombi's surfaces by the blood flow. From these results, we observed that it is the thrombus shell that experiences the highest fluid-induced shear stresses on its surface. A combination of the two results, namely that the shell is both weaker and experiences more deformation, leads to the conclusion that it is the most prone to embolism. The implications of this finding are that a new class of anti-embolic drugs could be developed, which would target the dissolution of the shell selectively, while preventing the risk of severe bleeding (typically associated with the existing antithrombotic medications) by leaving the core of the clots intact. Finally, we have laid down a foundation for a nondimensionalization approach to interpreting thrombogenesis data, with the hope that a uniform theory could be developed through an extension of this procedure. Overall, the findings herein are expected to be beneficial to understanding the process of thrombogenesis which is central to heart attacks and strokes that are plaguing the public health today.

6. Codes and Data Sharing

The codes used for this work can be found at <https://git.njit.edu/rvoronov/lbm>. The raw data is too large (> 1 TB) for web repository storage. Instead, it is hosted on supercomputing tape storage at <https://portal.tacc.utexas.edu/user-guides/ranch>, and is provided upon request.

7. Acknowledgements

We would like to thank the Prof. Skip Brass laboratory (including Prof. Timothy J. Stalker and Dr. John D. Welsh) at the University of Pennsylvania's Perelman School of Medicine for performing all the experiments and sharing their microscopy data. Also, we acknowledge that a part of this work was initiated under the guidance of Prof. Scott L. Diamond at the University of Pennsylvania Department of Chemical and Biomolecular Engineering, and Bioengineering Institute for Medicine & Engineering.

The study was financially supported by the New Jersey Health Foundation Grant #PC101-17, and in part by NIH R01-HL103419 "Blood Systems Biology" grant and AHA 11POST6890012 Postdoctoral Fellowship. Undergraduate labor was supported by Shodor's Blue Waters 2018-2019 Student Internship Program.

We also acknowledge that computational resources were provided by the National Center for Supercomputing Applications (NCSA) at the University of Illinois at Urbana-Champaign, Texas Advanced Computing Center (TACC) at the University of Texas at Austin; Allocations: TG-BCS170001 and TG-BIO160074 by the Extreme Science and Engineering Discovery Environment (XSEDE)[91], which is supported by National Science Foundation grant number ACI-1548562.

8. Disclosure statement

The authors have no competing financial interests to declare.

References

1. Xu, J., et al., Deaths: Final Data for 2016. *National Vital Statistics Report*, 2018. **67**(5): p. 1-76.
2. Benjamin, E.J., et al., Heart Disease and Stroke Statistics—2017 Update: A Report From the American Heart Association. *Circulation*, 2017. **135**(10): p. e146-e603.
3. Johnson, S., et al., Review of Mechanical Testing and Modelling of Thrombus Material for Vascular Implant and Device Design. *Annals of Biomedical Engineering*, 2017. **45**(11): p. 2494-2508.
4. Stalker, T.J., et al., Hierarchical organization in the hemostatic response and its relationship to the platelet-signaling network. *Blood*, 2013. **121**(10): p. 1875.
5. Falati, S., et al., Real-time in vivo imaging of platelets, tissue factor and fibrin during arterial thrombus formation in the mouse. *Nature Medicine*, 2002. **8**(10): p. 1175-1180.
6. Flaumenhaft, R., Thrombus formation reimaged. *Blood*, 2014. **124**(11): p. 1697-1698.
7. Fogelson, A.L. and K.B. Neeves, Fluid Mechanics of Blood Clot Formation. *Annual review of fluid mechanics*, 2015. **47**: p. 377-403.
8. Wang, W.W. and M.R. King, Multiscale Modeling of Platelet Adhesion and Thrombus Growth. *Annals of Biomedical Engineering*, 2012. **40**(11): p. 2345-2354.
9. Chueh, J.Y., et al., Mechanical Characterization of Thromboemboli in Acute Ischemic Stroke and Laboratory Embolus Analogs. *American Journal of Neuroradiology*, 2011. **32**(7): p. 1237.
10. Teng, Z., et al., Layer- and Direction-Specific Material Properties, Extreme Extensibility and Ultimate Material Strength of Human Abdominal Aorta and Aneurysm: A Uniaxial Extension Study. *Annals of Biomedical Engineering*, 2015. **43**(11): p. 2745-2759.
11. Gasser, T.C., et al., Failure properties of intraluminal thrombus in abdominal aortic aneurysm under static and pulsating mechanical loads. *Journal of Vascular Surgery*, 2008. **48**(1): p. 179-188.
12. O'Leary, S.A., et al., The biaxial mechanical behaviour of abdominal aortic aneurysm intraluminal thrombus: Classification of morphology and the determination of layer and region specific properties. *Journal of Biomechanics*, 2014. **47**(6): p. 1430-1437.
13. Lee, Y.U., et al., Histological and Biomechanical Changes in a Mouse Model of Venous Thrombus Remodeling. *Biorheology*, 2015. **52**(3): p. 235-245.
14. van Dam, E.A., et al., Determination of linear viscoelastic behavior of abdominal aortic aneurysm thrombus. *Biorheology*, 2006. **43**(6): p. 695-707.
15. van Kempen, T.H.S., et al., A constitutive model for developing blood clots with various compositions and their nonlinear viscoelastic behavior. *Biomechanics and Modeling in Mechanobiology*, 2016. **15**: p. 279-291.
16. Slaboch, C.L., et al., Mechano-rheological properties of the murine thrombus determined via nanoindentation and finite element modeling. *Journal of the Mechanical Behavior of Biomedical Materials*, 2012. **10**: p. 75-86.
17. Chih-Chung, H., C. Pay-Yu, and S. Cho-Chiang, Estimating the viscoelastic modulus of a thrombus using an ultrasonic shear-wave approach. *Medical Physics*, 2013. **40**(4): p. 042901.
18. Xie, H., et al., Correspondence of ultrasound elasticity imaging to direct mechanical measurement in aging DVT in rats. *Ultrasound in Medicine & Biology*, 2005. **31**(10): p. 1351-1359.

19. Mfoumou, E., et al., Time-dependent hardening of blood clots quantitatively measured in vivo with shear-wave ultrasound imaging in a rabbit model of venous thrombosis. *Thrombosis Research*, 2014. **133**(2): p. 265-271.
20. Voronov, R.S., et al., Simulation of intrathrombus fluid and solute transport using in vivo clot structures with single platelet resolution. *Annals of Biomedical Engineering*, 2013. **41**(6): p. 1297-1307.
21. Topalov, N.N., et al., Two Types of Procoagulant Platelets Are Formed Upon Physiological Activation and Are Controlled by Integrin alpha(IIb)beta(3). *Arteriosclerosis Thrombosis and Vascular Biology*, 2012. **32**(10): p. 2475-+.
22. Ruf, A. and H. Patscheke, Flow Cytometric Detection of Activated Platelets: Comparison of Determining Shape Change, Fibrinogen Binding, and P-Selectin Expression. *Seminars in Thrombosis and Hemostasis*, 1995. **21**(2): p. 146-151.
23. Chatterjee, M.S., et al., Pairwise agonist scanning predicts cellular signaling responses to combinatorial stimuli. *Nature Biotechnology*, 2010. **28**(7): p. 727-U1737.
24. Bark, D., A. Para, and D. Ku, Correlation of thrombosis growth rate to pathological wall shear rate during platelet accumulation. *Biotechnology and Bioengineering*, 2012. **109**(10): p. 2642-2650.
25. Wu, W.-T., et al., Multi-Constituent Simulation of Thrombus Deposition. *Scientific Reports*, 2017. **7**: p. 42720.
26. Bajd, F. and I. Serša, Mathematical Modeling of Blood Clot Fragmentation During Flow-Mediated Thrombolysis. *Biophysical Journal*, 2013. **104**(5): p. 1181-1190.
27. Tolouei, E., et al., Effect of Hemodynamic Forces on Platelet Aggregation Geometry. *Annals of Biomedical Engineering*, 2011. **39**(5): p. 1403-1413.
28. Tosenberger, A., et al., Modelling of platelet–fibrin clot formation in flow with a DPD–PDE method. *Journal of Mathematical Biology*, 2016. **72**(3): p. 649-681.
29. Yazdani, A., et al., A General Shear-Dependent Model for Thrombus Formation. *PLOS Computational Biology*, 2017. **13**(1): p. e1005291.
30. Pinar, I.P., et al., Methods to Determine the Lagrangian Shear Experienced by Platelets during Thrombus Growth. *PLOS ONE*, 2015. **10**(12): p. e0144860.
31. Xu, Z., et al., A multiscale model of thrombus development. *Journal of The Royal Society Interface*, 2008. **5**(24): p. 705-722.
32. Govindarajan, V., et al., Computational Study of Thrombus Formation and Clotting Factor Effects under Venous Flow Conditions. *Biophysical Journal*, 2016. **110**(8): p. 1869-1885.
33. Xu, S., et al., Model predictions of deformation, embolization and permeability of partially obstructive blood clots under variable shear flow. *Journal of The Royal Society Interface*, 2017. **14**(136).
34. Tokarev, A., et al., *Continuous mathematical model of platelet thrombus formation in blood flow*, in *Russian Journal of Numerical Analysis and Mathematical Modelling*. 2012. p. 191.
35. Kim, O.V., et al., Fibrin networks regulate protein transport during thrombus development. *PLOS Computational Biology*, 2013. **9**(6): p. e1003095.
36. Hiroki, K., et al., A three-dimensional particle simulation of the formation and collapse of a primary thrombus. *International Journal for Numerical Methods in Biomedical Engineering*, 2010. **26**(3-4): p. 488-500.
37. Skorczewski, T., Lindsay C. Erickson, and A.L. Fogelson, Platelet Motion near a Vessel Wall or Thrombus Surface in Two-Dimensional Whole Blood Simulations. *Biophysical Journal*, 2013. **104**(8): p. 1764-1772.
38. Pivkin, I.V., P.D. Richardson, and G. Karniadakis, Blood flow velocity effects and role of activation delay time on growth and form of platelet thrombi. *Proceedings of the National Academy of Sciences of the United States of America*, 2006. **103**(46): p. 17164-17169.
39. Wang, W., N.A. Mody, and M.R. King, Multiscale model of platelet translocation and collision. *Journal of Computational Physics*, 2013. **244**: p. 223-235.

40. Flamm, M.H., et al., Multiscale prediction of patient-specific platelet function under flow. *Blood*, 2012. **120**(1): p. 190-198.
41. Flamm, M.H., et al., Multiscale prediction of patient-specific platelet function under flow. *Blood*, 2012. **120**(1): p. 190-198.
42. Dolan, A.T. and S.L. Diamond, Systems modeling of Ca²⁺ homeostasis and mobilization in platelets mediated by IP₃ and store-operated Ca²⁺ entry. *Biophysical journal*, 2014. **106**(9): p. 2049-2060.
43. Taylor, J.O., et al., In Vitro Quantification of Time Dependent Thrombus Size Using Magnetic Resonance Imaging and Computational Simulations of Thrombus Surface Shear Stresses. *Journal of Biomechanical Engineering*, 2014. **136**(7): p. 071012-071012-11.
44. Colace, T., R. Muthard, and S.L. Diamond, Thrombus growth and embolism on tissue factor-bearing collagen surfaces under flow: Role of thrombin with and without fibrin. *Arteriosclerosis, Thrombosis, and Vascular Biology*, 2012. **32**(6): p. 1466-1476.
45. Wang, W., et al., Analysis of early thrombus dynamics in a humanized mouse laser injury model. *Biorheology*, 2014. **51**(1): p. 3-14.
46. Welsh, J.D., et al., A systems approach to hemostasis: 1. The interdependence of thrombus architecture and agonist movements in the gaps between platelets. *Blood*, 2014. **124**(11): p. 1808-1815.
47. Falati, S., et al., Real-time in vivo imaging of platelets, tissue factor and fibrin during arterial thrombus formation in the mouse. *Nat Med*, 2002. **8**(10): p. 1175-81.
48. Borders, J.L. and H.J. Granger, An Optical Doppler Intravital Velocimeter. *Microvascular Research*, 1984. **27**(1): p. 117-127.
49. Granger, D.N., et al., Leukocyte Adherence to Venular Endothelium during Ischemia-Reperfusion. *American Journal of Physiology*, 1989. **257**(5): p. G683-G688.
50. Davis, M.J., Determination of Volumetric Flow in Capillary Tubes Using an Optical Doppler-Velocimeter. *Microvascular Research*, 1987. **34**(2): p. 223-230.
51. Schindelin, J., et al., Fiji: an open-source platform for biological-image analysis. *Nature Methods*, 2012. **9**: p. 676.
52. Thevenaz, P., U.E. Ruttimann, and M. Unser, A pyramid approach to subpixel registration based on intensity. *IEEE Transactions on Image Processing*, 1998. **7**(1): p. 27-41.
53. Li, K., K. Li, "The image stabilizer plugin for ImageJ. 2008.
54. Succi, S., The lattice Boltzmann equation for fluid dynamics and beyond. *Numerical mathematics and scientific computation*. 2001, New York: Clarendon Press ; Oxford University Press. xvi, 288 p.
55. Sukop, M.C., D.T. Thorne, and NetLibrary Inc., *Lattice Boltzmann modeling an introduction for geoscientists and engineers*. 2006, Springer: Berlin ; New York. p. ix, 172 p.
56. Chen, S. and G.D. Doolen, Lattice Boltzmann method for fluid flows. *Annual Review of Fluid Mechanics*, 1998. **30**: p. 329-364.
57. Wang, J.Y., et al., Domain-decomposition method for parallel lattice Boltzmann simulation of incompressible flow in porous media. *Physical Review E*, 2005. **72**(1): p. 016706-11.
58. Kandhai, D., et al., Lattice-Boltzmann hydrodynamics on parallel systems. *Computer Physics Communications*, 1998. **111**(1): p. 14-26.
59. Cosgrove, J.A., et al., Application of the lattice Boltzmann method to transition in oscillatory channel flow. *Journal of Physics a-Mathematical and General*, 2003. **36**(10): p. 2609-2620.
60. Boyd, J., J. Buick, and S. Green, A second-order accurate lattice Boltzmann non-Newtonian flow model. *Journal of Physics a-Mathematical and General*, 2006. **39**(46): p. 14241-14247.
61. Yoshino, A., et al., A numerical method for incompressible non-Newtonian fluid flows based on the lattice Boltzmann method. *Journal of Non-Newtonian Fluid Mechanics*, 2007. **147**(1-2): p. 69-78.
62. Gabbanelli, S., G. Drazer, and J. Koplik, Lattice Boltzmann method for non-Newtonian (power-law) fluids. *Physical Review E*, 2005. **72**(4): p. 046312-7.

63. Swift, M.R., et al., Lattice Boltzmann simulations of liquid-gas and binary fluid systems. *Physical Review E*, 1996. **54**(5): p. 5041-5052.
64. Voronov, R., *Fluid Shear Stress and Nutrient Transport effects via Lattice-Boltzmann and Lagrangian Scalar Tracking Simulations of cell culture media perfusion through artificial bone engineering constructs imaged with microCT*[PhD Thesis], in *School of Chemical, Biological and materials Engineering*. 2010, University of Oklahoma. p. 131.
65. Porter, B., et al., 3-D computational modeling of media flow through scaffolds in a perfusion bioreactor. *Journal of Biomechanics*, 2005. **38**(3): p. 543-549.
66. VanGordon, S.B., et al., Effects of Scaffold Architecture on Preosteoblastic Cultures under Continuous Fluid Shear. *Industrial & Engineering Chemistry Research*, 2011. **50**(2): p. 620-629.
67. Voronov, R.S., et al., Efficient Lagrangian scalar tracking method for reactive local mass transport simulation through porous media. *International Journal for Numerical Methods in Fluids*, 2011. **67**(4): p. 501-517.
68. Voronov, R., et al., Computational modeling of flow-induced shear stresses within 3D salt-leached porous scaffolds imaged via micro-CT. *Journal of Biomechanics*, 2010. **43**(7): p. 1279-86.
69. Papavassiliou, D.V., et al., Chapter 23 - Lattice Boltzmann Methods for Bioengineering Applications, in *Numerical Methods and Advanced Simulation in Biomechanics and Biological Processes*. 2018, Academic Press. p. 415-429.
70. Williams, C., et al., Time-Dependent Shear Stress Distributions during Extended Flow Perfusion Culture of Bone Tissue Engineered Constructs. *Fluids*, 2018. **3**(2): p. 25.
71. Kadri, O.E., et al., Numerical Accuracy Comparison of Two Boundary Conditions Commonly used to Approximate Shear Stress Distributions in Tissue Engineering Scaffolds Cultured under Flow Perfusion. *International Journal for Numerical Methods in Biomedical Engineering*, 2018. **34**(11): p. e3132.
72. Wang, J., et al., Domain-decomposition method for parallel lattice Boltzmann simulation of incompressible flow in porous media. *Physical Review E*, 2005. **72**(1): p. 016706.
73. Alam, T.A., et al., Image-based modeling: A novel tool for realistic simulations of artificial bone cultures. *TECHNOLOGY*, 2016. **04**(04): p. 229-233.
74. Pham, N.H., et al., Bulk stress distributions in the pore space of sphere-packed beds under Darcy flow conditions. *Physical Review E: Statistical Nonlinear Soft Matter Physics*, 2014. **89**(3): p. 033016.
75. Pham, N.H., et al., Predicting the stress distribution within scaffolds with ordered architecture. *Biorheology*, 2012. **49**(4): p. 235-247.
76. Qian, Y.H., D. Dhumieres, and P. Lallemand, Lattice Bgk Models for Navier-Stokes Equation. *Europhysics Letters*, 1992. **17**(6bis): p. 479-484.
77. Bhatnagar, P.L., E.P. Gross, and M. Krook, A Model for Collision Processes in Gases .1. Small Amplitude Processes in Charged and Neutral One-Component Systems. *Physical Review*, 1954. **94**(3): p. 511-525.
78. Windberger, U., et al., Whole blood viscosity, plasma viscosity and erythrocyte aggregation in nine mammalian species: reference values and comparison of data. *Experimental Physiology*, 2003. **88**(3): p. 431-440.
79. Merrill, E.W. and G.A. Pelletie, Viscosity of Human Blood - Transition from Newtonian to Non-Newtonian. *Journal of Applied Physiology*, 1967. **23**(2): p. 178-182.
80. Kim, M.B. and I.H. Sarelius, Distributions of wall shear stress in venular convergences of mouse cremaster muscle. *Microcirculation*, 2003. **10**(2): p. 167-178.
81. Lipowsky, H.H., Microvascular rheology and hemodynamics. *Microcirculation*, 2005. **12**(1): p. 5-15.
82. Desjardins, C. and B.R. Duling, Microvessel Hematocrit - Measurement and Implications for Capillary Oxygen-Transport. *American Journal of Physiology*, 1987. **252**(3): p. H494-H503.

83. Sriram, K., M. Intaglietta, and D.M. Tartakovsky, Non-Newtonian Flow of Blood in Arterioles: Consequences for Wall Shear Stress Measurements. *Microcirculation (New York, N.Y. : 1994)*, 2014. **21**(7): p. 628-639.
84. Kheifets, V.O., et al., Patient-Specific Computational Modeling of Blood Flow in the Pulmonary Arterial Circulation. *Computer Methods and Programs in Biomedicine*, 2015. **120**(2): p. 88-101.
85. Lipowsky, H.H., S. Kovalcheck, and B.W. Zweifach, The distribution of blood rheological parameters in the microvasculature of cat mesentery. *Circulation research*, 1978. **43**(5): p. 738-749.
86. Nesbitt, W.S., et al., A shear gradient-dependent platelet aggregation mechanism drives thrombus formation. *Nature Medicine*, 2009. **15**(6): p. 665-U146.
87. Sakariassen, K.S., et al., Shear-induced platelet activation and platelet microparticle formation in native human blood. *Thrombosis Research*, 1998. **92**(6): p. S33-S41.
88. Holme, P.A., et al., Shear-induced platelet activation and platelet microparticle formation at blood flow conditions as in arteries with a severe stenosis. *Arteriosclerosis Thrombosis and Vascular Biology*, 1997. **17**(4): p. 646-653.
89. Westerhof, N., N. Stergiopulos, and M.I.M. Noble, *Snapshots of Hemodynamics*. 2 ed. 2010, USA: Springer US. XIV, 272.
90. Taylor, J.O., et al., Development of a computational model for macroscopic predictions of device-induced thrombosis. *Biomechanics and Modeling in Mechanobiology*, 2016. **15**(6): p. 1713-1731.
91. Towns, J., et al., XSEDE: accelerating scientific discovery. *Computing in Science & Engineering*, 2014. **16**(5): p. 62-74.

ACCEPTED MANUSCRIPT

Highlights

- Image-based modeling is used to calculate the fluid-induced forces responsible for yielding deformation of clots formed in mice.
- The results show that clot yielding occurs mostly in clot outer shell while its inner core is intact.
- The results also show that data for all clots follow a uniform trajectory when non dimensionalized.